Improved Operation and Control of Single-Phase Integrated On-Board Charger System

Jialou Gao, *Student Member, IEEE*, Wei Sun, *Member, IEEE*, Dong Jiang, *Senior Member, IEEE*, Yuanzhi Zhang, *Student Member, IEEE*, and Ronghai Qu, *Fellow, IEEE*

***Abstract*—Single-phase grid-connected integrated on-board charger (IOBC) can significantly reduce the cost and the bulk of electric vehicles and has been used in real products. However, there are still two problems that have not been discussed and solved. First, when permanent magnet synchronous motor drives are used for single-phase IOBC, there are second-order current harmonic and the possibility of instability in the system. Second, when multiphase motor (MPM) drives are used for single-phase IOBC, the currents' assignment strategy and the dc voltage utilization of inverter need to be dissected. This article does detailed research works about these two problems. The origin of the second-order harmonic and the instability are exposed. Furthermore, proportional-double-resonant regulator and adaptive proportional (P) parameter control schemes are proposed to solve these problems. The operation principle of single-phase IOBC with MPM drive is analyzed. Two different operating modes are recommended, and an optimal zero-sequence voltage is designed to increase the dc voltage utilization capability of the inverter. At last, the feasibility of the proposed operation and control schemes are verified by experiments.**

***Index Terms*—Current control, electric vehicles (EV), integrated charger, permanent magnet synchronous motor (PMSM).**

I. Introduction

ELECTRIC vehicles (EV) have been rapidly promoted and developed in recent years due to their several significant benefits, such as reduced greenhouse gas emissions and superior vehicular performance [1]. As the critical technique for supplying electric energy to EV's battery, the charging technique has also attracted great attention [2]. Off-board chargers are significant infrastructures for EV. They can provide a high-power level charging function. However, off-board chargers can only be used in some specific places, so that they lack charging flexibility and convenience. Conversely, on-board chargers (OBC) can be used in anywhere with grid outlets. However, their power levels are limited due to additional cost and volume.

Manuscript received February 26, 2020; revised May 21, 2020 and July 30, 2020; accepted September 10, 2020. Date of publication September 21, 2020; date of current version November 20, 2020. This work was supported in part by the Natural Science Foundation of China under Grant 51807077 and in part by the grants from the Power Electronics Science and Education Development Program of Delta Group (DREG2018002). Recommended for publication by Associate Editor G. De Donato. *(Corresponding author: Wei Sun.)*

The authors are with the Department of Electrical and Electronics, Huazhong University of Science and Technology, Wuhan 430074, China (e-mail: m201871417@hust.edu.cn; sunwei198677@hotmail.com; jiangd@hust.edu.cn; yzzhang@hust.edu.cn; ronghaiqu@hust.edu.cn).

Color versions of one or more of the figures in this article are available online at https://ieeexplore.ieee.org.

Digital Object Identifier 10.1109/TPEL.2020.3025664

The ac motor drive and pulsewidth modulation rectifier have similarities from the aspect of power conversion. Therefore, integrated on-board chargers (IOBC), which utilize motor drive to construct the hardware of OBC, were investigated in [3]–[14]. In IOBC, motor windings act as filter inductance, and the propulsion inverter is used as an ac/dc converter or a dc/dc converter of the charger. Therefore, the cost and volume of the power electronic system of EV can be significantly reduced by implementing IOBC. In future high power OBC technologies, IOBC will be quite an effective solution [2].

There are kinds of methods that have been proposed to realize the integrated charger. First, three-phase grid-connected IOBC are reviewed. In [3] and [4], additional three-phase current source converters (CSC) were used to interface with the three-phase grid. Motor windings and propulsion inverter act as a boost dc/dc converter. In charging mode, the motor will not generate torque. However, CSC still consume some space and cost. In [5]–[7], six-phase motor drives were reconstructed to connect to a three-phase grid, and the structure was similar to a parallel converter. Meanwhile, the synthetic magnetomotive force (MMF) is pulsating along a fixed axis, so that the electromagnetic torque is zero. In [8]–[10], multiphase motor (MPM) drives with prime number phases were used for the integrated charger. The principle of those methods is similar to the six-phase motor drive. Practically, the three-phase grid is usually used in industry and is not common in residence or other public occasions. Moreover, three-phase permanent magnet synchronous motor (PMSM) drives, which are the most popular in EV application, have no practical solutions to realize three-phase charging functions, unless adding extra power electronics units [3], [4].

Three-phase PMSM drives can easily achieve single-phase grid-connected IOBC. In [11], a single-phase integrated charger circuit was introduced and is illustrated in Fig. 1. During charging, the phase-a winding of PMSM is connected to one side of the single-phase grid, whereas the phase-a leg of the inverter is connected to another side. The currents have relationship of Fig. 2 ($i_a = -2i_b = -2i_c$). A pulsating MMF along a-axis is produced. Furthermore, if the d-axis of PMSM is aligned to a-axis, the electromagnetic torque will be zero. In [12], a diode bridge was added to rectify the grid, and the three-phase motor drive acts as a boost dc/dc converter. There is no need for hardware reconfiguration. Similar to [11], the MMF is also pulsating along the d-axis of PMSM, and torque can be eliminated. In [13], MPM drives were used, and zero-torque IOBC

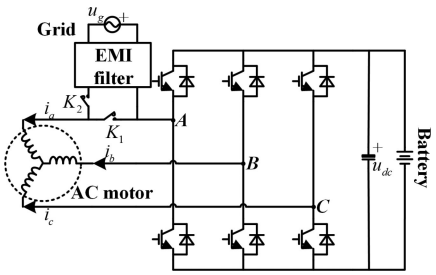

Fig. 1. Schematic circuit diagram of the studied single-phase IOBC.

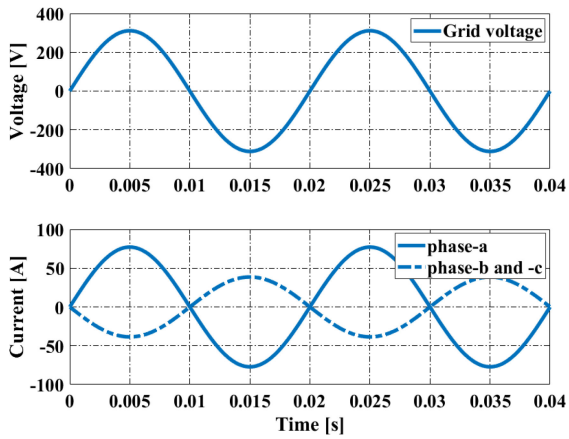

Fig. 2. Current waveforms of single-phase IOBC during charging.

can be achieved by only feeding zero-sequence current into the motor. However, the motor's neutral point should be pulled out. In [14], a four-phase switched reluctance motor drive was used to construct a single-phase integrated charger. There are no additional devices. It is cheap and robust. However, it will generate torque during charging.

Compared to three-phase integrated chargers, single-phase integrated chargers are more practical to apply in EV. Despite the structures of single-phase integrated chargers are plenty, there is a common feature that the pulsating armature MMF is along the *d*-axis of PMSM. Due to the effect of permanent magnet (PM), the magnetic path of the armature field will be periodically saturated, and the equivalent inductance will be time-variant as a result. The time-variant inductance will result in two control problems. The first problem is the second-order current harmonic, and the second problem is that the phase margin of the control system will reduce a lot when the equivalent inductance gets small. The typical proportional–resonant (PR) controller cannot solve the above problems [11]. This article analyzes the origin of the above issues and proposes an improved control scheme to solve them. Without loss of generality, the charging circuit shown in Fig. 1 is chosen to discuss the saturation principle and to design corresponding solutions in this article.

On the other hand, the integrated circuits proposed in [11] and [12] can also extend to the MPM drives, and the motor does not need to be modified. However, the operation of the circuits with MPM drives is different from the circuits with three-phase drives. First, there are more current combinations in the multiphase system. Besides, the dc voltage of the inverter should be larger than twice the peak value of the grid voltage if there is no improved operation scheme, which means a higher risk of overmodulation. This article proposes two operating modes for the single-phase IOBC system with MPM drive, one for minimizing the power loss and the other for eliminating the torque. Moreover, the effect of zero-sequence voltage (V_0) on the modulation is dissected in this article, and the optimal V_0 is proposed to prevent the inverter from overmodulation.

TABLE I
PARAMETERS OF THE SIMULATIONAL IPMSM

Items	Values (Units)
Slots/Poles	48/8
Rated power	70 kW
Stator outer diameter	264 mm
Stator inner diameter	162 mm
Rated speed	4000 rpm
Peak Power	120 kW
Max. phase current	240 Arms

The rest of this article is organized as follows. In Sections II and III, the analysis of single-phase integrated chargers (incorporating with PMSM and MPM drives, respectively) is presented. The corresponding control and operation problems are explained. In Section IV, improved control and operation schemes are proposed to solve these problems. In Section V, experiments are used to verify the proposed methods. Finally, Section VI concludes this article.

II. Analysis of Single-Phase Integrated Charger Incorporating With PMSM Drives

The schematic circuit diagram of the studied IOBC is shown in Fig. 1. Electromagnetic interference (EMI) filter is always necessary for grid-tied converters and is used for suppressing the high-frequency common-mode (CM) and differential-mode (DM) EMI. The typical overheads of EMI filter for the power level of 12–20 kW are one- or two-stage *LC* filters (Typical value: $L_{\rm cm}$: 1 mH, $C_{\rm cm}$: 3 μF, $L_{\rm dm}$: 165 μH, $C_{\rm dm}$: 17.6 nF), their volume and cost are relatively small [15]. It should be noted that other single-phase IOBCs have similar electromagnetic characteristics to the studied one. Therefore, the discussion in this article can be extended to other single-phase IOBC systems. In this section, loss and thermal of the single-phase IOBC are evaluated by simulation since the loss and the temperature rise are controversial issues in the IOBC system. The theoretical analysis of the loss and of the temperature rise is beyond the scope of this article. Subsequently, the single-phase IOBC with PMSM drive is analyzed in detail.

A. Thermal Evaluation of Single-Phase IOBC

A 70-kW three-phase interior PMSM (IPMSM), which is suitable for EV application, is simulated with FEM software to evaluate the loss and the temperature rise of the motor in the charging mode. The parameters of the IPMSM are listed in Table I.

Three modes have been simulated. The first mode is the single-phase charging mode, the charging power is 12 kW, and the

TABLE II
LOSSES OF IPMSM UNDER CHARGING AND PROPULSION MODE

Loss \ Mode	12 kW charging mode	Drive mode with phase current 54.55Arms	Drive mode with rated output power
Magnet eddy current loss	7.5 W	0.38 W	0.79 W
Stator core loss	2.928 W	223.67 W	283.19 W
Rotor core loss	0.94 W	20.06 W	30.85 W
Copper loss	180.2 W	360 W	798.5 W

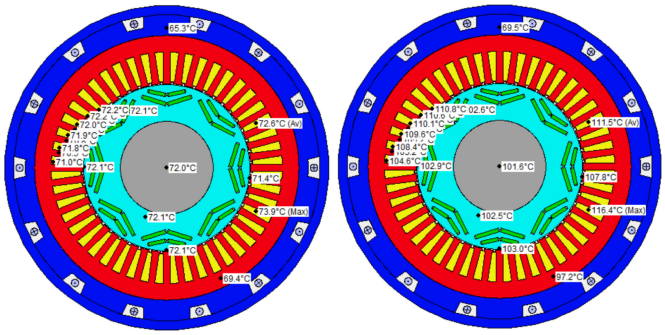

Fig. 3. Temperature distribution of (a) charging mode and (b) propulsion mode.

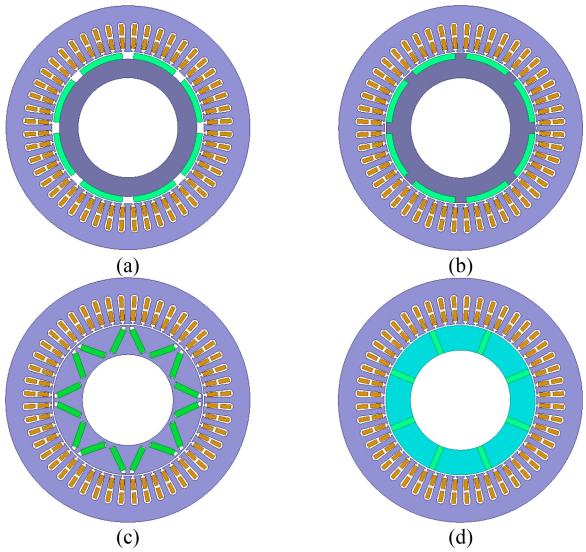

Fig. 4. Four mainstream PMSM topologies used in EV. (a) Surface-mounted PMSM. (b) Inserted PMSM. (c) V-shaped IPMSM. (d) I-shaped IPMSM.

current of the grid-tied phase equals 54.55 Arms. The second mode is propulsion mode, the speed is 4000 r/min, and the rms value of each phase current is equal to 54.55 Arms (100 N·m torque is produced). The last mode is propulsion mode with rated output power, and the speed is 4000 r/min. The PM eddy current loss, copper loss, and core loss under those three modes have been calculated, and the results are presented in Table II.

Furthermore, the temperature rise of IPMSM was also simulated with MotorCAD software. The outer housing cooling is natural convection, whereas the inner housing cooling is water cooling. The ambient temperature is 40°, the inlet temperature of the cooling water is 65°, and the flow rate is 8 L/min. The winding ends are filled with thermally conductive glue. The temperature distribution of IPMSM under 12 kW charging mode and under propulsion mode (rated power) is shown in Fig. 3(a) and (b), respectively.

Obviously, under a similar cooling condition, the temperature rise of IPMSM in 12 kW charging mode is significantly lower than the propulsion mode. Hence, single-phase IOBC has no concerns about high-temperature demagnetization of PM or overheating of the motor.

B. d-Axis Inductance Variation of Single-Phase IOBC Incorporating With PMSM Drive

As mentioned in Section I, to eliminate the torque, only the *d*-axis armature reaction field is generated in single-phase IOBC incorporating with PMSM drive. Actually, the combined effect of the *d*-axis armature reaction field and PM field can cause the saturation of material and result in inductance variation. The design of the controller is closely related to the value of inductance. Hence, the *d*-axis inductance variation should be dissected.

Generally speaking, the PMSMs applied in EV are radial-field machines with the internal rotor, and the PM is on the rotor. Fig. 4 shows four mainstream PMSM topologies [16]. The magnetic path of the *d*-axis armature field will be different depending on the PMSM topology. As a result, the reason for magnetic saturation will also have a discrepancy.

Surface-mounted PMSM [Fig. 4(a)] and inserted PMSM [Fig. 4(b)] place the PM on rotor surface. Therefore, there is little leakage flux of the PM, and the magnetic path of the *d*-axis armature reaction field will be equivalent to the magnetic path of the PM main field [16]. The magnetic path includes the stator tooth (reluctance $R_{\rm st}$), stator yoke and rotor yoke (reluctance R_y), and two air gaps (reluctance $2R_g$). The relationship between the inductance and the reluctance is shown in (1), where N is the equivalent turns of windings

$$L_{\rm SPMSM} = \frac{N^2}{R_{\rm st} + R_y + 2R_g} \tag{1}$$

$$L_{\rm IPMSM} = \frac{N^2}{R_l + R_{\rm st} + R_y + 2R_g}. \tag{2}$$

Usually, the PM will make the stator tooth near the inflection point of the magnetization curve. Fig. 5 shows the principle, F_m is the MMF of PM. In the charging mode, *d*-axis armature reaction MMF (F_a) will make the stator tooth get into saturation region periodically. Therefore, the inductance will vary with *d*-axis current (F_a is proportional to i_d). Specifically, when $i_d > 0$, the inductance will decrease because the stator tooth gets into saturated region; when $i_d < 0$, the inductance will increase since the stator tooth gets into linear region. Fig. 6 shows an FEM simulation result of a typical SPMSM.

IPMSM [see Fig. 4(c)] accommodates the PM within the rotor, and there is leakage flux produced by PM. Meanwhile,

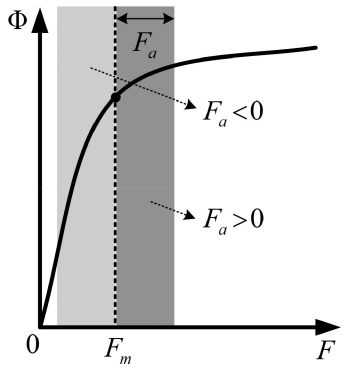

Fig. 5. Magnetization curve of stator tooth.

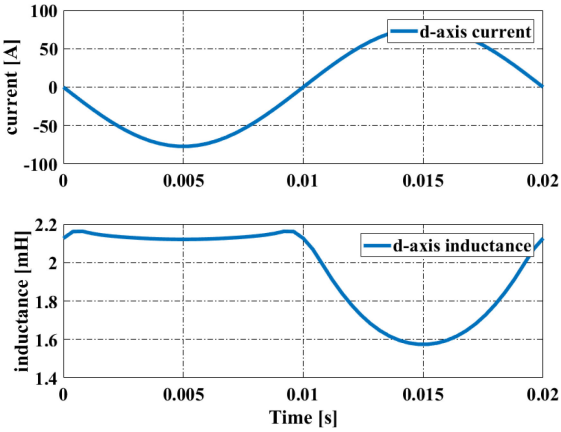

Fig. 6. Curve of d-axis inductance for SPMSM.

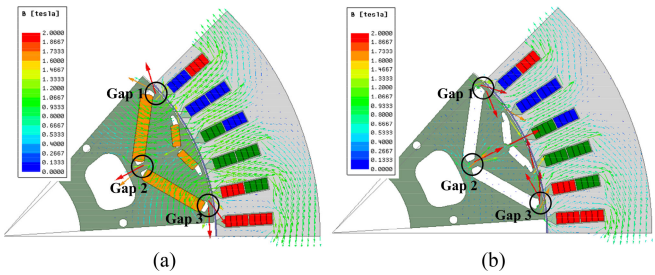

Fig. 7. (a) Magnet field excited only by PM ($F_a = 0$). (b) Armature reaction field ($F_m = 0$, $F_a > 0$).

the armature reaction field will not path through the PM [16]. Hence, the magnetic path of the d-axis armature field will not only include stator tooth and stator yoke, but also include the magnetic path in which the PM leakage field exists (reluctance R_l). Fig. 7 shows the above situation. The gaps are the magnetic path in which the PM leakage field exists. R_l is larger than R_{st} and R_y (the gaps are narrower than stator tooth and yoke). Therefore, the inductance of IPMSM will be mainly determined by R_l and R_g. The gaps are so narrow that even the PM leakage field can make the gaps near the saturated region of the material. On the other hand, it can be found from Fig. 7(b) that, when $i_d > 0$, the d-axis armature reaction field is in the opposite direction to

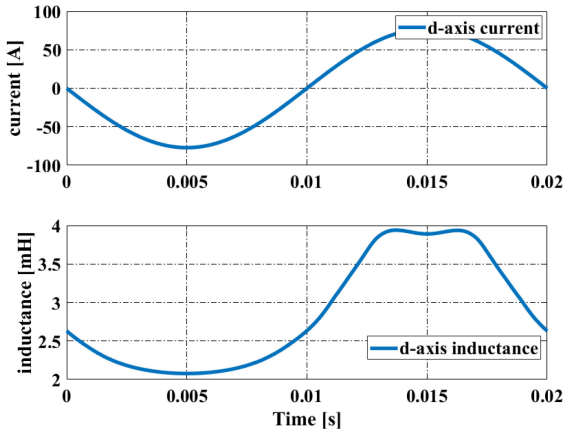

Fig. 8. Curve of d-axis inductance for IPMSM.

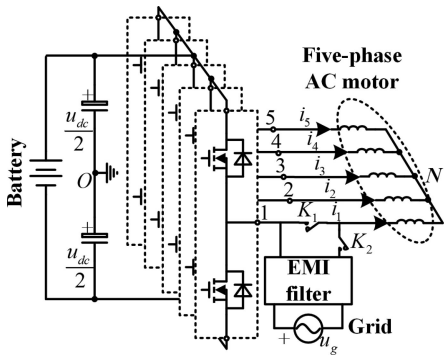

Fig. 9. Single-phase IOBC incorporating with five-phase motor drive.

the PM leakage field in those gaps. Therefore, when $i_d > 0$, the inductance will increase since the gaps get into the linear region; when $i_d < 0$, the inductance will decrease since the gaps get into the saturation region. Fig. 8 shows an FEM simulation result of an IPMSM.

As for rotor topology shown in Fig. 4(d), the PM leakage field will path through the air gap, and the magnetic path of the PM leakage field will not get into the saturation region. Therefore, the inductance variation is similar to the case of surface-mounted PMSM.

The time variation of d-axis inductance will influence the steady-state and transient process of current control. The detailed analysis will be described in Section IV.

III. Analysis of Single-Phase Integrated Charger Incorporating With MPM Drives

MPMs have the advantages of better fault tolerance and high-power rating. MPM and their drives may become serious contenders for future EV applications [17]. Single-phase charging function can also be integrated into MPM drives. Fig. 9 shows an example of single-phase IOBC with a five-phase motor drive.

A. Operating Modes of Single-Phase IOBC With MPM Drives

As shown in Fig. 9, the current of the grid-connected phase (assuming i_1) is determined by the power command. The sum of currents of other phases is equal to $-i_1$. The assignment way of other phases currents affects the loss and the torque of the single-phase IOBC. Generally speaking, the currents of other phases are in-phase or antiphase to i_1 (for eliminating the torque). Hence, the ratios of them are the freedom of control. Two modes are proposed in this article.

The first mode minimizes the switching loss of inverter (proportional to currents' amplitude) and the copper loss of motor (proportional to currents' square), whereas the armature reaction field and the torque are not considered. Equation (3) shows the currents constrain equation and the optimization goals of the first mode; n is the phase number of MPM

$$\begin{cases} \text{currents constrain} \begin{cases} i_1 = I_g \sin(\omega_g t + \varphi_g) \\ i_2 + i_3 + \cdots + i_n = -i_1 \end{cases} \\ \begin{cases} i_2 = k_2 i_1, i_3 = k_3 i_1, \ldots, i_n = k_n i_1 \\ k_2, k_3, .., k_n = \arg\min\left\{i_1^2 + i_2^2 + i_3^2 + \cdots + i_n^2\right\} \text{ and} \\ \arg\min\left\{|i_1| + |i_2| + |i_3| + \cdots + |i_n|\right\}. \end{cases} \end{cases} \tag{3}$$

According to triangle inequality, the second optimization goal can be achieved when $i_2, i_3, \ldots, i_n$ have the same sign. On the other hand, according to linear algebra theory, the first optimization goal can be achieved when $i_2 = i_3 = \cdots = i_n$. Therefore, the first operating mode has global minimum switching loss and global minimum copper loss if $i_2 = i_3 = \cdots = i_n = -i_1/(n-1)$.

However, according to the coordinate transformation of the multiphase system [18], there is pulsating armature MMF excited in flux/torque plane. Equation (4) shows the principle. As a result, the rotor should be assigned to a specific position (α-axis) for eliminating the torque. Moreover, the pulsating armature MMF will also result in PM eddy current loss

$$\begin{cases} i_{\alpha 1} = \frac{2}{n}\sum_{k=1}^{n} i_k \cos\frac{2(k-1)\pi}{n} = \frac{2i_1}{n-1} \\ i_{\beta 1} = \frac{2}{n}\sum_{k=1}^{n} i_k \sin\frac{2(k-1)\pi}{n} = 0. \end{cases} \tag{4}$$

The second mode doesn't generate MMF in the flux/torque plane so that the torque is zero, and the PM eddy current loss can be reduced. Equation (5) shows the currents constrain equation and two optional optimization goals for the second mode. Numerical optimization methods are needed to solve the above equation, which is beyond the scope of this article. As an example, for the five-phase motor, one solution of (5) is $i_2 = i_5 = -0.809 i_1$, $i_3 = i_4 = 0.309 i_1$

$$\begin{cases} \text{currents constrain} \begin{cases} i_1 = I_g \sin(\omega_g t + \varphi_g) \\ i_2 + i_3 + \cdots + i_n = -i_1 \\ \sum_{k=1}^{n} i_k \cos\frac{2(k-1)\pi}{n} = 0 \\ \sum_{k=1}^{n} i_k \sin\frac{2(k-1)\pi}{n} = 0 \end{cases} \\ \begin{cases} i_2 = k_2 i_1, i_3 = k_3 i_1, \ldots, i_n = k_n i_1 \\ k_2, k_3, .., k_n = \arg\min\left\{i_1^2 + i_2^2 + i_3^2 + \cdots + i_n^2\right\} \text{ or} \\ \arg\min\left\{|i_1| + |i_2| + |i_3| + \cdots + |i_n|\right\}. \end{cases} \end{cases} \tag{5}$$

TABLE III
LOSSES OF SIX-PHASE PMSM AND THREE-PHASE PMSM IN CHARGING MODE

Loss \ Mode	MPM: the first mode @12 kW	MPM: the second mode @ 12 kW	Three-phase PMSM @ 12 kW
Magnet eddy current loss	1.75 W	0.15 W	7.5 W
Stator core loss	0.7 W	1.7 W	2.928 W
Rotor core loss	0.25 W	0.27 W	0.94 W
Copper loss	72.5 W	250.7 W	180.2 W

B. Loss Analysis of Single-Phase IOBC With MPM Drive

The copper loss of a n-phase motor working in the first mode can be calculated by (6). Even if assuming that the resistance of the MPM is equal to the resistance of the three-phase motor, the copper loss of the MPM is still less than the three-phase motor. But actually, MPM usually has smaller resistance than the three-phase motor, which will decrease the copper loss further. On the other hand, it can be found from (4) that the armature magnetic-excitation of MPM is also weaker than the three-phase motor. Therefore, the PM eddy current loss will also be less than the three-phase motor

$$P_{Cu} = \sum_{k=1}^{n} i_k^2 R_s = \frac{n i_1^2 R_s}{n-1}. \tag{6}$$

The second mode produces tiny PM eddy current loss because the generated MMF is very weak (MMF equals to zero theoretically). The copper loss of the second mode will be larger than the first mode because some phases' current may increase. However, the copper loss of the second mode is still comparable to the three-phase motor.

Similar to Section II-A, losses of a six-phase PMSM have been calculated by FEM software. In the simulation, the only difference between the six-phase PMSM and the three-phase PMSM is the winding distribution. The three-phase winding is separated into a six-phase winding. Besides, the currents of MPM have a relationship of $i_2 = -1.4 i_1$, $i_3 = i_1$, $i_4 = i_5 = i_6 = -0.2 i_1$ in the second mode.

Table III lists the simulation results. When MPM works in the second mode, the PM eddy current loss reduces a lot. The core loss of MPM is less than the three-phase motor no matter which mode is selected. MPM has less copper loss when it works in the first mode. The copper loss of MPM working in the second mode is a little bit larger than the three-phase motor. However, the current level in charging mode is undoubtedly less than the drive mode. Therefore, the cooling condition of the stator is great enough to prevent MPM from overheating. Finally, it can be concluded that the single-phase IOBC incorporating with MPM drive also has no concerns about high-temperature demagnetization of PM or overheating of the motor.

C. DC Voltage Utilization of Single-Phase IOBC

At present, the dc voltage level of most EV on the market is around 400 V, and it will develop to higher voltage [19]. According to the typical discharge curve of the battery, the minimum battery voltage in the nominal working area is 85.7% of the rated voltage [20]. Therefore, the normal range of dc

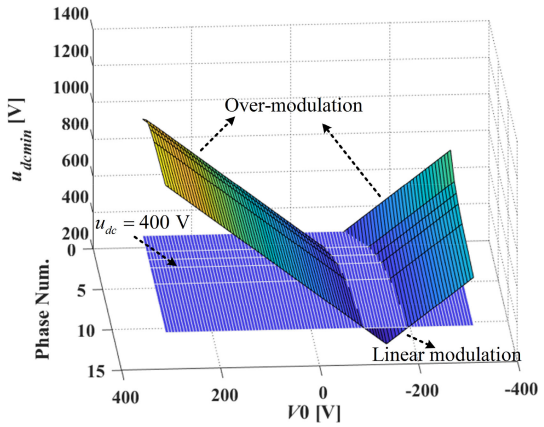

Fig. 10. Relationship between phase number V_0 and the minimum requirement of dc voltage.

voltage is between 340–400 V, which means a single-phase grid can be directly connected to the inverter. However, for some hybrid EV (HEV) whose battery voltage is lower than 311 V, a bidirectional boost dc/dc regulator is needed. This dc/dc regulator can also expand the speed range of HEV [21]. The participation of the dc/dc converter has little influence on the studied charger system, provided a reasonable synergistic control strategy is applied. In the synergistic control strategy, the real-time charging or discharging power is feedforward to the controller of the dc/dc converter simultaneously. The dc-link voltage can maintain the desired level (340–400 V) even the charging power has a sudden change [22].

The dc voltage utilization of single-phase IOBC refers to the lowest dc voltage of the system for working in the linear modulation region. Obviously, the dc voltage requirement of single-phase IOBC should not exceed 340–400 V

$$\boldsymbol{L}\begin{bmatrix} pi_1 \\ pi_2 \\ \vdots \\ pi_n \end{bmatrix} + R_s \begin{bmatrix} i_1 \\ i_2 \\ \vdots \\ i_n \end{bmatrix} = \begin{bmatrix} u_{1O} \\ u_{2O} \\ \vdots \\ u_{nO} \end{bmatrix} - \begin{bmatrix} u_g \\ 0 \\ \vdots \\ 0 \end{bmatrix} - \begin{bmatrix} u_{NO} \\ u_{NO} \\ \vdots \\ u_{NO} \end{bmatrix} \tag{7}$$

$$\boldsymbol{L}\begin{bmatrix} pi_1 \\ pi_2 \\ \vdots \\ pi_n \end{bmatrix} + R_s \begin{bmatrix} i_1 \\ i_2 \\ \vdots \\ i_n \end{bmatrix} = \begin{bmatrix} u_{1O} \\ u_{2O} \\ \vdots \\ u_{nO} \end{bmatrix} - \begin{bmatrix} \frac{n-1}{n}u_g \\ -\frac{u_g}{n} \\ \vdots \\ -\frac{u_g}{n} \end{bmatrix} - \begin{bmatrix} V_0 \\ V_0 \\ \vdots \\ V_0 \end{bmatrix}. \tag{8}$$

In order to analyze the dc voltage utilization, the model of single-phase IOBC with MPM drive (see Fig. 9) is derived, as shown in (7). Since the sum of currents is zero, u_{NO} equals $(u_{1O}+u_{2O}+\cdots+u_{nO}-u_g)/n$. Thus, model (8) can be obtained, where $V_0=(u_{1O}+u_{2O}+\cdots+u_{nO})/n$.

In steady-state, the voltage drop on the inductor and the resistance can be neglected. Therefore, the phase-leg output voltage u_{kO} ($k=1,2,\ldots,n$) of the inverter is related to phase number, and V_0 (V_0 is the zero-sequence voltage of inverter and can be set to any value artificially). The dc voltage should be larger than twice the peak of u_{kO}. Fig. 10 shows the relationship among phase number V_0 and the minimum requirement of dc voltage (u_{dcmin}, for working in the linear region). It can be found that when dc voltage is 400 V, the selection of V_0 determines whether the inverter operates in the linear modulation region or overmodulation region. In the typical method, V_0 is set to zero, but it can be seen that the inverter will get into the overmodulation zone when the phase number increases. In order to improve the performance of single-phase IOBC, the best choice of V_0 will be discussed in Section IV, and it will ensure that the inverter can always work in the linear region (with 340 V dc voltage and any phase number).

IV. Improved Control and Operation Scheme

In this section, control schemes for single-phase IOBCs incorporating with three-phase and MPM drive are proposed, especially for single-phase IOBCs with three-phase PMSM drive and MPM drive. For the integrity of design, the control method for single-phase IOBC with a three-phase induction motor (IM) drive is also introduced.

A. Control for Single-Phase IOBC With IM Drive

IM is also a commonly used motor type in EV. IM will not produce torque when it is applied in the single-phase IOBC. The mathematic model of IM in $\alpha\beta$-frame ($\omega_r=0$) is shown in (9). R_s and R_r are the resistance of phase-winding of the stator and the rotor, respectively. L_s and L_r are the self-inductance of the stator and the rotor, respectively. M_m is the mutual inductance. n_p is the pole pairs. The transfer function between $i_{r\alpha}$ ($i_{r\beta}$) and $i_{s\alpha}$ ($i_{s\beta}$) can be obtained as (10). If the ratio of $i_{s\beta}$ and $i_{s\alpha}$ is controlled to a constant, the torque of IM will be zero according to the torque equation of IM, which means that only magnetic-excitation current exists in IM while there is no torque-generation current. In the single-phase IOBC with the three-phase motor, $i_{s\beta}$ is always controlled to zero. Therefore, the torque of IM is zero because the ratio of $i_{s\beta}$ and $i_{s\alpha}$ is zero

$$\begin{cases} \begin{bmatrix} u_{s\alpha} \\ u_{s\beta} \\ 0 \\ 0 \end{bmatrix} \overset{\omega_r=0}{=} \begin{bmatrix} R_s+sL_s & 0 & sM_m & 0 \\ 0 & R_s+sL_s & 0 & sM_m \\ sM_m & 0 & R_r+sL_r & 0 \\ 0 & sM_m & 0 & R_r+sL_r \end{bmatrix} \\ \qquad\qquad \times \begin{bmatrix} i_{s\alpha} \\ i_{s\beta} \\ i_{r\alpha} \\ i_{r\beta} \end{bmatrix} \\ T_e = 1.5n_pM_m\left(i_{s\beta}i_{r\alpha}-i_{s\alpha}i_{r\beta}\right) \end{cases} \tag{9}$$

$$\frac{i_{r\alpha}}{i_{s\alpha}} = \frac{i_{r\beta}}{i_{s\beta}} = \frac{-sM_m}{R_r+sL_r}, (\omega_r=0) \tag{10}$$

$$\psi_\alpha = M_m\left(i_{s\alpha}+i_{r\alpha}\right) = \frac{M_m\left(R_r+sL_{lr}\right)}{R_r+sL_r}i_{s\alpha} \approx \frac{M_mL_{lr}}{L_r}i_{s\alpha}. \tag{11}$$

On the other hand, the flux in air gap can be calculated by (11). It can be seen that the magnetic-excitation of the charging

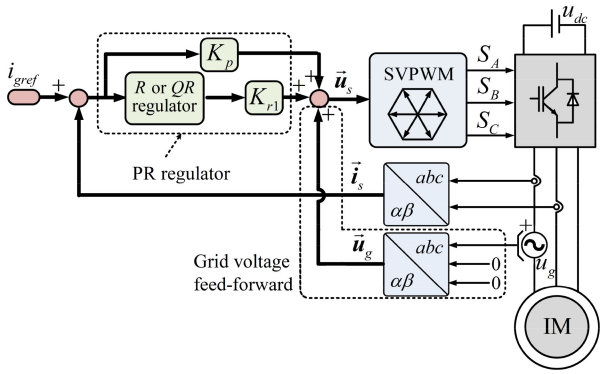

Fig. 11. Complex vector control diagram of current controller for single-phase IOBC incorporating with IM drive.

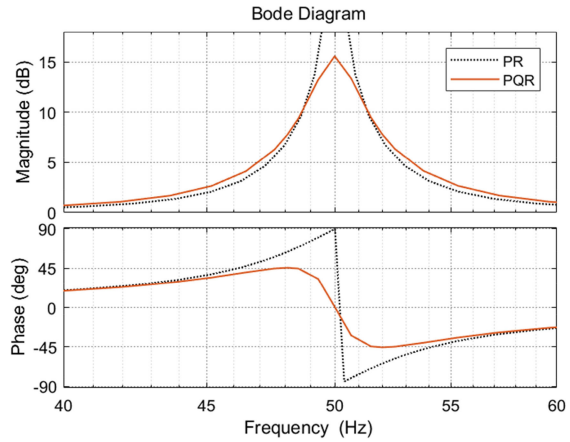

Fig. 12. Bode diagram of PR and PQR regulator ($K_p = 1$, $K_{r1} = 50$, $\omega_{c1} = 5$ rad/s).

mode is weaker than the drive mode (the equivalent magnetic-excitation inductance of drive mode is equal to M_m). The grid current can be up to L_r/L_{lr} times of the rated excitation current of IM, whereas the stator and the rotor will not get into magnetic saturation region. Therefore, single-phase IOBC incorporating with three-phase IM will not have the problems of periodical magnetic saturation.

Hence, current controller based on PR regulator can be used for single-phase IOBC incorporating with IM drive. Fig. 11 shows the complex vector control diagram. The control targets are controlling current vector to pulsate at α-axis. The reference of β-axis current equals zero. The α-axis current reference is ac quantity at the grid frequency. Therefore, PR regulator should be used to track the references with no steady-state error [23]

$$G_{PR}(s) = K_p + \frac{K_{r1}s}{s^2 + (\omega_g)^2} \tag{12}$$

$$G_{PQR}(s) = K_p + \frac{K_{r1}s}{s^2 + 2\omega_{c1}s + (\omega_g)^2}. \tag{13}$$

The transfer function of the ideal PR regulator is expressed as (12), and the Bode diagram is shown in Fig. 12 [23]. The R regulator has infinite gain at its resonant frequency ω_g. Generally, ω_g should be accurately calculated via the grid phase-lock loop, and the value of ω_g should feedback to the PR regulator in real time. Besides, in order to reduce the sensitivity toward slight deviation of grid frequency, a component with the cutoff frequency of ω_{c1} is inserted into the resonant part of the ideal PR regulator [23], and this type of nonideal PR regulator is called proportional quasi-resonant (PQR) regulator, which is usually used in practice. The transfer function of the PQR regulator is expressed as (13), and the Bode diagram is shown in Fig. 12. Compared with the typical PR regulator, the PQR regulator has a higher gain in the frequency band near the resonant frequency. Therefore, even if there is a small deviation in grid frequency, the controller's gain at grid frequency remains a relatively large value, and the controller can track the ac reference without error. For the specific digital implementation of PR or PQR regulator, please refer to the literature [24].

Grid voltage feedforward control law (14) is used to improve the ability to suppress grid disturbance. This article uses constant amplitude coordinate transformation so that the feedforward coefficient equals 2/3

$$\vec{u}_g = \frac{2u_g}{3}. \tag{14}$$

The parameters of the controller can be tuned as the following recommendation. Assuming that the equivalent inductance of phase winding of IM is $L_{\rm eq}$, the resistance is R_s, and the switching cycle is T_s. The needed bandwidth of the current control loop is ω_c (rad/s). Subsequently, K_p can be set to $\omega_c L_{\rm eq}$, and K_{r1} can be set to $\omega_c R_s$. With the above parameters, the open-loop transfer function of the current control loop is (15), which takes the time delay ($1.5T_s$) caused by discrete control into account. Therefore, the phase margin of the system (in rad) can be calculated by (16). Then, ω_c can be selected by (16) according to the needed phase margin. On the other hand, ω_{c1} of PQR regulator ranges from 1 to 10 rad/s generally [23]

$$G_{op}(s) = \left(\omega_c L_{\rm eq} + \frac{\omega_c R_s s}{s^2 + 2\omega_{c1}s + \omega_g^2}\right) \cdot \frac{e^{-1.5T_s s}}{sL_{\rm eq} + R_s} \tag{15}$$

$$\mathrm{PM} = \frac{\pi}{2} - 1.5\omega_c T_s. \tag{16}$$

B. Improved Control for Single-Phase IOBC With PMSM Drive

As analyzed in Section II-B, when PMSM drive is used, the d-axis inductance will change with d-axis current. Therefore, the d-axis voltage equation of single-phase IOBC with PMSM drive can be expressed as (17), where u_{id} is the d-axis voltage of inverter and u_{gd} is the d-axis voltage of the grid.

Only considering the average inductance and the first-order inductance variation, the d-axis inductance can be expressed as (18) in which k_{L-i} is the proportion factor. According to the analysis in Section II-B, k_{L-i} is positive if IPMSM drive is used and is negative if surface-mounted PMSM drive is used. Substituting (18) into (17) obtains (19) with which the d-axis

current can be solved

$$\left(\frac{dL_d\left(i_d\right)}{di_d}i_d + L_d\left(i_d\right)\right)\frac{di_d}{dt} + R_s i_d = u_{id} - u_{gd} \tag{17}$$

$$L_d\left(i_d\right) = L_{d0} + k_{L-i}\cdot i_d \tag{18}$$

$$\left(L_{d0} + 2k_{L-i}\cdot i_d\right)\frac{di_d}{dt} + R_s i_d = u_{id} - u_{gd}. \tag{19}$$

In steady-state, the d-axis current should equal the grid current ($I_g\sin(\omega_g t)$). The voltage equation in the steady-state can be deduced to (20). U_{gd} is the grid voltage, and the radial frequency of the grid is ω_g. The inverter should output second-order component to counteract with the second-order harmonic generated by inductance variation. Otherwise, second-order current harmonics will be produced. Traditional PR controller can only track the fundamental harmonic while cannot eliminate this second-order harmonics. In grid standards, there are total harmonic distortion (THD) requirements and restrictions on low-order harmonics. Therefore, the traditional PR controller needs to be improved

$$\begin{aligned}&\omega_g L_{d0} I_g\cos\left(\omega_g t\right) + 2\omega_g k_{L-i} I_g^2\sin\left(2\omega_g t\right)\\ &+ I_g R_s\sin\left(\omega_g t\right) = U_{id} - U_{gd}.\end{aligned} \tag{20}$$

To solve the problem of the steady-state harmonic, a proportional-double-resonant (P-DR) regulator is used in this article. The transfer function of the P-DR regulator is expressed in (21). There are two quasi-resonant regulators in the P-DR regulator. The first quasi-resonant regulator has a resonant frequency at grid frequency and is utilized to track the ac reference without steady-state error. The second quasi-resonant regulator has a resonant frequency at the double grid frequency and is used to compensate for the second-order harmonics caused by inductance variation

$$\begin{aligned}G_{\mathrm{P-DR}}\left(s\right) = K_p &+ \frac{K_{r1}s}{s^2 + 2\omega_{c1}s + \left(\omega_g\right)^2}\\ &+ \frac{K_{r2}s}{s^2 + 2\omega_{c2}s + \left(2\omega_g\right)^2}\end{aligned} \tag{21}$$

$$\left(L_{d0} + 2k_{L-i}\cdot I_d\right)\frac{d\tilde{i}_d}{dt} + R_s\tilde{i}_d = \tilde{u}_{id} - \tilde{u}_{gd}. \tag{22}$$

On the other hand, since IOBC is a single-phase system, the controller is usually executed in the stationary coordinate system. Therefore, the working point of the control plant is time-varying. The instantaneous equivalent inductance determines the instantaneous inertia of the control plant. Hence inductance variation may cause an unstable problem or damage the dynamic response performance of the control system. The small signal model of the d-axis voltage equation is expressed as (22), where I_d is the d-axis current of the instantaneous working point.

The instantaneous inertia of the control plant will vary with the instantaneous working point. When using the traditional PR controller, the parameters of PR regulators are constant. Fig. 13 shows the open-loop and closed-loop Bode diagram of the system in two different working points, and the traditional controller is used. It can be found that the phase margin of the system will decrease a lot when the inductance decreases, which

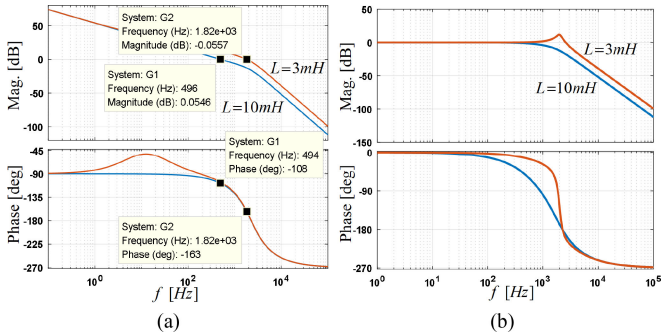

Fig. 13. Bode diagrams with different equivalent inductances but with similar PR parameters. (a) Open loop. (b) Closed loop.

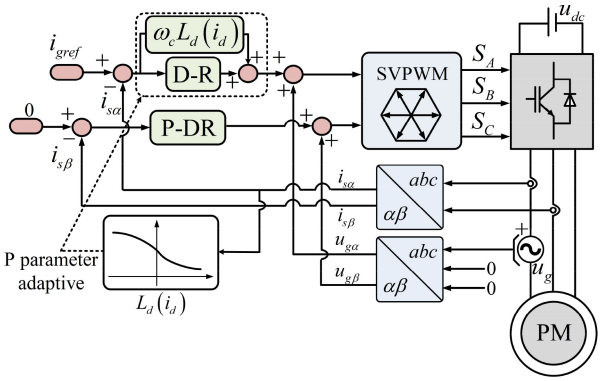

Fig. 14. Current controller based on P-DR regulator and P parameter adaptive algorithm for IMDCS with PMSM drive.

will destroy the control performance or even make the system unstable.

This article proposes an adaptive proportional (P) parameter algorithm to solve the problem of periodically decrease of phase margin. The inertia of the plant will decrease when the equivalent inductance gets smaller. Since the P parameter of the regulator determines the transient speed of the controller, if the P parameter is not changing with the instantaneous inertia of the plant, the inertia of the whole control system will be influenced by the time-varying inertia of the plant, then the control performance will be destroyed. However, if the P parameter changes synchronously with system instantaneous inertia, the control performance will be maintained in the whole working range.

Generally, the P parameter is equal to cutoff angular frequency multiplies equivalent inductance ($\omega_c L_{\mathrm{eq}}$). This article proposes that the P parameter of the regulator in d-axis control path changes with the instantaneous equivalent inductance $L_d(i_d)$, which can maintain the inertia of the whole control system, and the control performance can be maintained. The control diagram is shown in Fig. 14, where D-R represents the double-resonant regulator. The curves of instantaneous equivalent inductance $L_d(i_d)$ can be measured offline discretely, and the continuous curve can be obtained by interpolation. The curves of $L_d(i_d)$ will be used online.

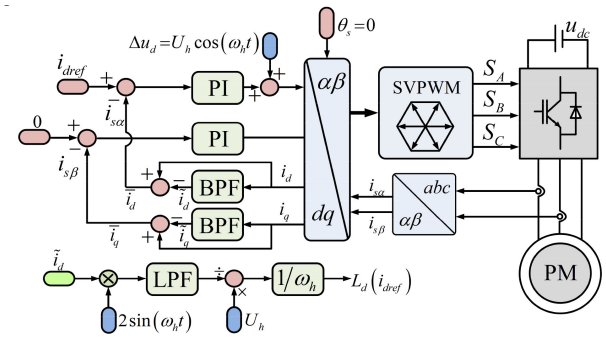

Fig. 15. Offline inductance measure method based on pulsated high-frequency signal injection (BPF: bandpass filter; LPF: low-pass filter).

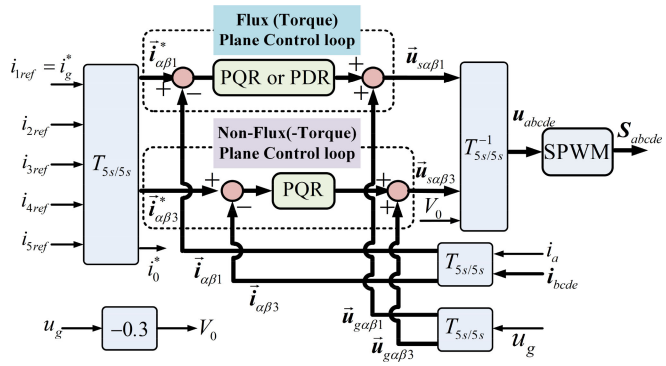

Fig. 16. Current controller for single-phase IOBC with five-phase motor drive.

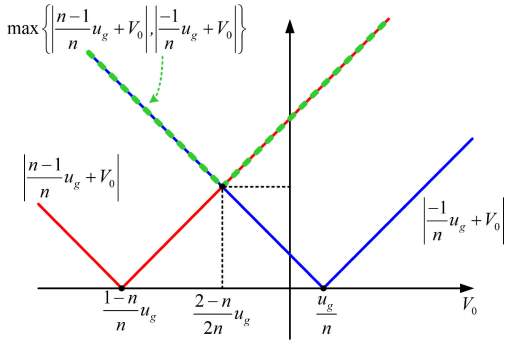

Fig. 17. Graphical method for finding the optimal V_0.

For regulator in the d-axis control loop (d-axis is aligned to α-axis), the proportional regulator equals $\omega_c L_d(i_d)$, in which ω_c is the needed bandwidth and is designed according to (16). The sum of K_{r1} and K_{r2} equals $\omega_c R_s$, the ratio of K_{r1} and K_{r2} determines whether better fundamental harmonic tracking capability or better second-harmonic eliminating capability. Generally, the ratio of K_{r1} and K_{r2} can be set to 3/2. As for ω_{c1} and ω_{c1}, empirical value (1–10 rad/s) can be chosen. For the regulator in the q-axis (β-axis) control loop, the proportional parameter equals $\omega_c L_q$, and other parameters can be the same as that of the d-axis regulator.

Finally, the recommended offline measuring method is illustrated in Fig. 15. A pulsed high-frequency signal injection is used. BPF is a bandpass filter to extract the injected frequency component of current. The amplitude of the injected frequency component of the d-axis current is calculated by multiplying with $2\sin(\omega_h t)$ and filtering the high-frequency components. θ_r in Fig. 15 is equal to zero.

C. Improved Control for Single-Phase IOBC With MPM Drive

In this article, only odd phase number MPM is discussed for avoiding confusion. But the proposed controller has the versatility and can be easily promoted to even phase number MPM.

The decoupling transformation matrix is usually used in the multiphase system [18]. The actual currents and the references are all transformed into flux/torque subplane, nonflux/torque subplane, and zero-axis. The inductance variation should be considered in the flux/torque subplane if a multiphase PMSM drive is used. Since there is no neutral point in MPM, the zero-axis control loop can be omitted

$$T_{5s/5s} = \frac{2}{5}\begin{bmatrix} \cos(\alpha) & \cos(2\alpha) & \cos(3\alpha) & \cos(4\alpha) & \cos(5\alpha) \\ -\sin(\alpha) & -\sin(2\alpha) & -\sin(3\alpha) & -\sin(4\alpha) & -\sin(5\alpha) \\ \cos(3\alpha) & \cos(6\alpha) & \cos(9\alpha) & \cos(12\alpha) & \cos(15\alpha) \\ -\sin(3\alpha) & -\sin(6\alpha) & -\sin(9\alpha) & -\sin(12\alpha) & -\sin(15\alpha) \\ 1/2 & 1/2 & 1/2 & 1/2 & 1/2 \end{bmatrix}. \tag{23}$$

As an example, the current controller of single-phase IOBC with five-phase motor drive is designed. Fig. 16 shows the control diagram. Five-phase decoupling transformation matrix $T_{5s/5s}$ is expressed in (23), where $\alpha = 2\pi/5$. The references are given according to the needed operating modes, which have been described in Section III-A. For instance, if the first operating mode is selected, $i_{2\mathrm{ref}} = i_{3\mathrm{ref}} = i_{4\mathrm{ref}} = i_{5\mathrm{ref}} = -0.25\, i_{1\mathrm{ref}}$; if the second operating mode is selected, $i_{2\mathrm{ref}} = i_{5\mathrm{ref}} = -0.809 i_{1\mathrm{ref}}$, and $i_{3\mathrm{ref}} = i_{4\mathrm{ref}} = 0.309 i_{1\mathrm{ref}}$. Meanwhile, the regulators in the flux/torque subplane are also determined by the operating modes. P-DR and adaptive proportional parameter algorithm should be used if the first mode is chosen, whereas the P-QR regulator can be used if working in the second mode. The methods of tuning the control parameters have been discussed in Sections IV-A and IV-B.

On the other hand, zero-axis voltage V_0 should be designed optimally to prevent the inverter from overmodulation. According to (8), optimal V_0 can minimize the maximum in $\{u_{1O}, u_{2O}, \ldots, u_{nO}\}$. Hence, the choice of V_0 should satisfy (24). Fig. 17 shows the graphical representation for selecting the optimal V_0. It is evident that when $V_0 = (2-n) * u_g/(2n)$, the maximum in $\{u_{1O}, u_{2O}, \ldots, u_{nO}\}$ has a minimum

$$V_0 = \arg\min\left(\max\left\{\left|\frac{n-1}{n}u_g + V_0\right|, \left|\frac{-1}{n}u_g + V_0\right|\right\}\right). \tag{24}$$

For instance, when using a five-phase motor drive, V_0 should equal minus $0.3u_g$. Subsequently, the peak of u_{kO} ($k = 1, 2, \ldots, 5$) will be twice $u_g/2$ in steady-state. The inverter can work in the linear modulation region even if the dc voltage equals 340 V. As

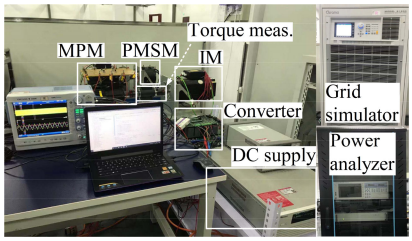

Fig. 18. Experimental platform.

TABLE IV
PARAMETERS OF GRID AND INVERTER

Symbol	Parameters	Value
u_g	Grid voltage in RMS value	220 V
f_g	Grid frequency	50 Hz
u_{dc}	DC-link voltage of inverter	400 V
f_{sw}	Switching frequency of inverter	20 kHz
V_{CES}	Collector-emitter voltage of IGBT	1200 V
$I_{C(nom)}$	Rated collector current of IGBT	100 A

TABLE V
PARAMETERS OF THE TESTED PMSM

Symbol	Parameters	Value
L_d	d-axis main inductance of PMSM	10.3 mH
L_q	q-axis main inductance of PMSM	10.7 mH
R_s	Resistance of windings of PMSM	0.1Ω
P_e	Rated power of PMSM	5.2 kW
n_p	Pole pairs of PMSM	3
n_{rpm}	Rated speed of IM	2000 rpm
I_e	Rated current	11.14 A

a comparison, if V_0 equals zero, the peak of u_{1O} equals $4u_g/5$ in steady state. Thus, the inverter will get into the overmodulation region when the grid voltage is 220 Vrms, and the dc voltage is 340 V.

V. EXPERIMENTAL RESULTS

Experimental tests were performed in a 2-kW test rig, and Fig. 18 shows the experimental platform. The instantaneous motor torque was measured during charging/discharging. The grid simulator outputs a 220 Vrms/50 Hz ac voltage. The dc-link voltage of the three-phase voltage source converter was 400 V. The switching frequency was 20 kHz. The IGBT module used in tests is Infineon FS100R12KE2. Due to the dc supply cannot feedback the power while the grid simulator can feedback the power, the following tests are all in discharging mode. In fact, charging and discharging processes are the same except for the direction of power transfer.

The parameters of the grid and inverter are summarized in Table IV, and the parameters of PMSM and MPM are summarized in Tables V and VI, respectively.

TABLE VI
PARAMETERS OF THE FIVE-PHASE IM

Symbol	Parameters	Value
L_m	Main inductance of MPM	203.3 mH
L_{lr}	Leakage inductance of MPM rotor	7.6 mH
L_{ls}	Leakage inductance of IM stator	14.8 mH
R_s	Resistance of MPM stator	1.1 Ω
R_r	Resistance of MPM rotor	0.9 Ω
n_{rpm}	Rated speed of MPM	1500 rpm

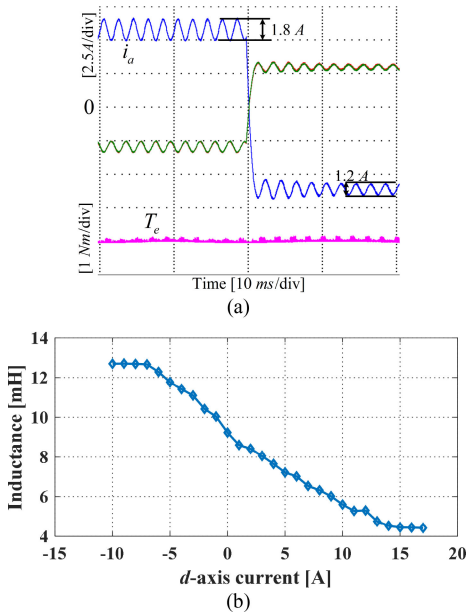

Fig. 19. (a) Inductance variation of single-phase IOBC with PMSM drive. (b) d-axis inductance curve.

A. Results of Single-Phase IOBC With PMSM Drive

As discussed in Section II-B, for single-phase IOBC with PMSM, the equivalent inductance will vary with d-axis current. Fig. 19(a) shows the currents waveform under conditions that the dc offset of d-axis current equals 6 or –6 A. A 500-Hz harmonic was injected into d-axis output voltages. It can be found that the equivalent impedance with 6 A dc offset is less than the equivalent impedance with –6 A dc offset. On the other hand, the results of the offline d-axis inductance measuring test are shown in Fig. 19(b).

The steady-state and transient procedure of single-phase IOBC with PMSM drive were tested. The bandwidth of the current controller was 500 Hz. Fig. 20(a) shows the waveforms in the starting procedure if using the traditional controller. Fig. 20(b) shows the waveforms if using the improved controller. It can be seen that the start process becomes faster if using the improved controller. Moreover, the overshoot is also less than the traditional controller, which means that the improved controller has better dynamic response performance.

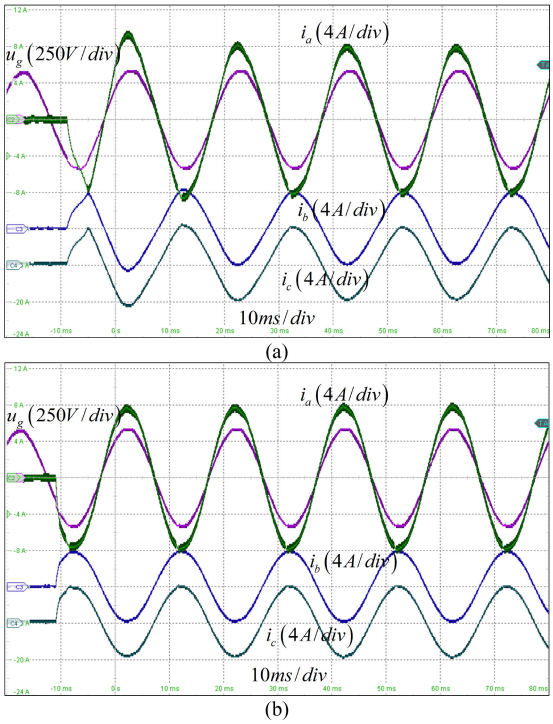

Fig. 20. Waveforms of single-phase IOBC with PMSM drive in the starting procedure (a) using traditional controller and (b) using the improved controller.

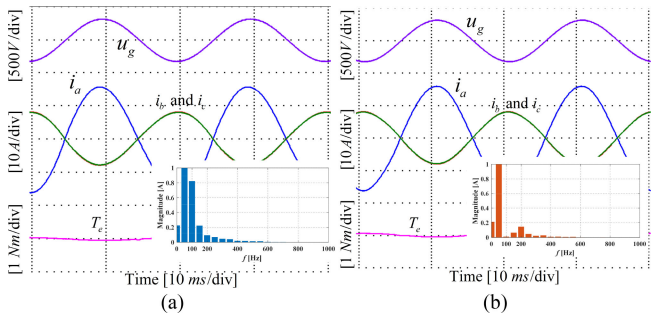

Fig. 21. (a) Waveforms in a steady state with PR regulator. (b) Waveforms in a steady state with P-DR regulator.

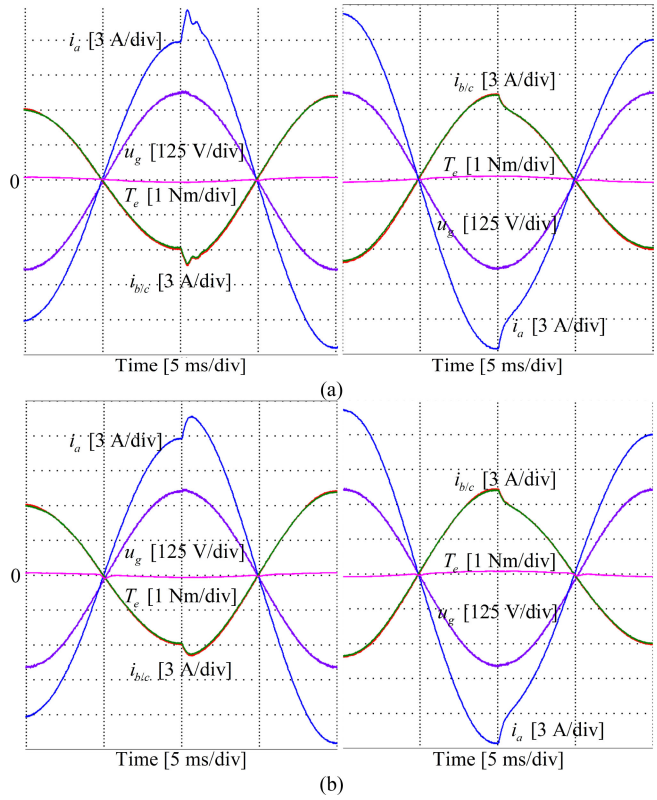

Fig. 22. Waveforms in transient process (a) without P parameter adaptive strategy and (b) with P parameter adaptive strategy.

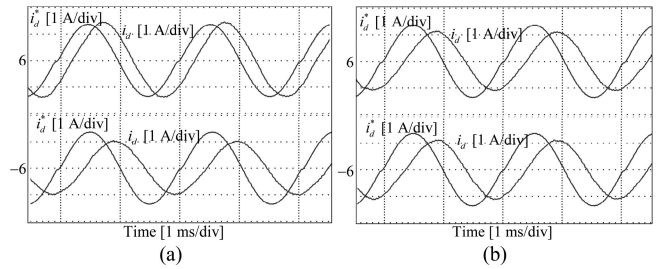

Fig. 23. Small signal tests (a) without P parameter adaptive strategy and (b) with P parameter adaptive strategy.

Fig. 21(a) shows the current waveforms in steady state with typical PR control strategy, and the fast Fourier transform analysis result of i_a is attached to the lower right corner. It can be seen that double main frequency harmonic, which is caused by inductance variation exists when using the PR controller. The amplitude of second-order current harmonic is 0.8 A and is 5% of the fundamental harmonic, whereas if using the proposed P-DR current controller, the second-order current harmonics can be eliminated, as shown in Fig. 21(b). Due to the tested PMSM has relatively large inductance, and the switching frequency of the inverter is set to 20 kHz, the current THD of both controllers are very low. In the actual grid converter, current THD should be lower than 5% according to grid standards. This article mainly considers the second-order harmonic suppression, and the methods to regulate the current THD can refer to other literature. Fig. 21 also shows that the torque is almost zero during charging. The small alternating torque is due to positioning errors. But it only causes very little noise.

Fig. 22(a) shows the results of the transient test of the controller without the P parameter adaptive strategy. It can be found that the currents have overshoot when the d-axis current is positive amplitude, whereas no overshoot if the d-axis current is negative amplitude, which means that the phase margin will be decreased when the d-axis current is positive. Fig. 22(b) shows the control performance of the proposed controller. It can be found that the overshoot is eliminating.

Furthermore, small-signal tests were carried out to prove that the proposed controller can maintain the stability margin of the system. In the small-signal test, the dc reference was set at 6 or –6 A, whereas the ac reference was set at 1.414 A/500 Hz. As shown by Fig. 23(a), if there is no adaptive parameter strategy, the closed-loop gain of the controller will be larger than one

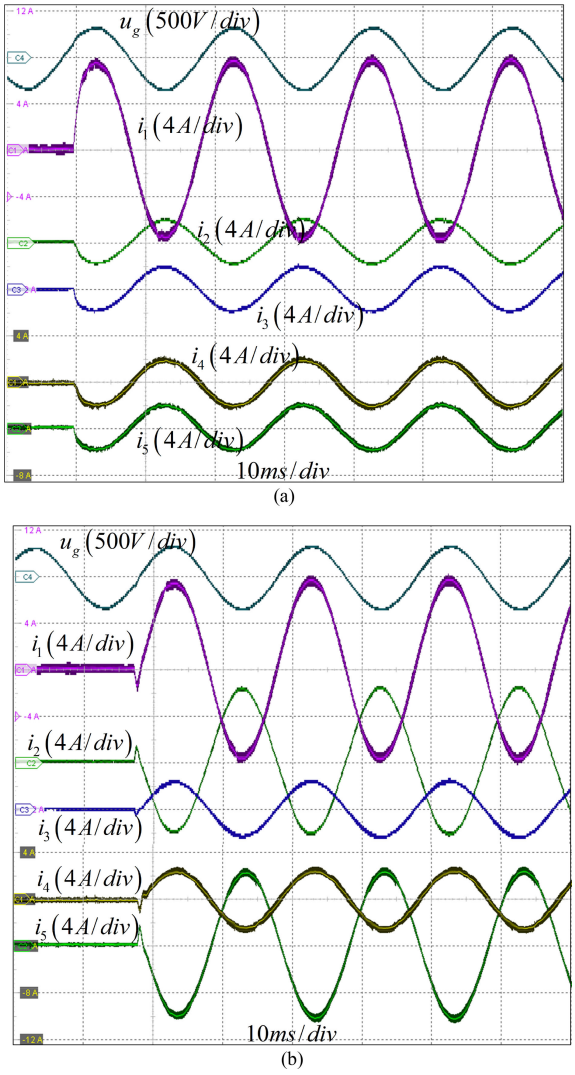

Fig. 24. Starting procedure of single-phase IOBC with MPM drive. (a) Waveforms of the first mode ($i_2 = i_3 = i_4 = i_5 = -0.25i_1$). (b) Waveforms of the second mode ($i_2 = i_5 = -0.809i_1$, $i_3 = i_4 = 0.309i_1$).

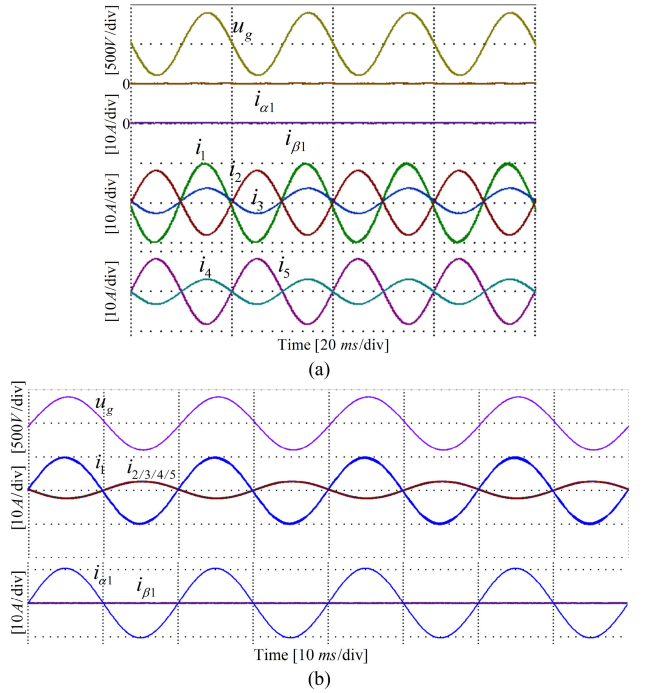

Fig. 25. Steady state of single-phase IOBC with MPM drive. (a) Waveforms of the second mode. (b) Waveforms of the first mode.

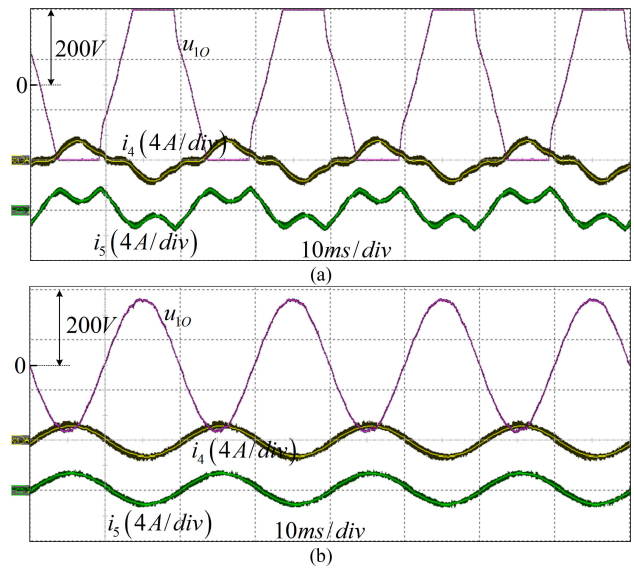

Fig. 26. Effect of zero-sequence voltage on single-phase IOBC with five-phase motor drive. (a) Zero-sequence voltage is equal to zero. (b) Zero-sequence voltage is equal to $-0.3u_g$.

when dc offset equals 6 A. And the closed-loop gain is 0.707 when dc offset equals –6 A. According to the mathematical relationship between open-loop transfer function and closed-loop transfer function, it can be extrapolated that the phase margin decreases about 30°. However, if using the proposed P parameter adaptive strategy, the phase margin can maintain constant, Fig. 23(b) proves the above conclusion.

B. Results of Single-Phase IOBC With MPM Drive

Tests for single-phase IOBC with MPM drive were also carried out. The parameters of the five-phase IM are shown in Table VI. Fig. 24(a) shows the waveforms in the starting procedure, and the MPM worked in the first mode. Fig. 24(b) shows the starting procedure of the second mode. It can be seen that the controllers have excellent transient performance.

Fig. 25 shows the waveforms in the steady state, and the current components in the flux/torque plane were calculated. It can be found that there is no excitation in the flux/torque producing plane if MPM works in the second mode ($i_{\alpha 1} = i_{\beta 1} = 0$). Fig. 25(b) shows the waveforms of the system working in the first mode ($i_2 = i_3 = i_4 = i_5 = -0.25i_1$). There is MMF generated in the α-axis of flux/torque producing plane.

Furthermore, the effect of the zero-sequence voltage has also been experimentally explored. Fig. 26 shows the experimental waveforms. The five-phase motor worked in the first mode, and the grid current was equal to 5 A. The required output voltage of the grid-tied leg of the inverter (u_{1O}) was exported from DSP by

a digital-to-analog converter. It can be seen that the inverter gets into the overmodulation region if $V_0 = 0$, and the currents have serious distortion. However, when a suitable V_0 is injected, the inverter will be linear modulated, and the currents are sinusoidal.

The above test results indicate that the proposed operation and control strategies for single-phase IOBC are effective. High quality, high integration, and zero-torque charging process can be achieved.

VI. Conclusion

This article has made detailed research works about the operation principle and control of the single-phase IOBC system. Four major conclusions can be summarized in this article as follows.

1) There is inductance variation in single-phase IOBC incorporating with PMSM drive. This inductance variation is caused by periodical saturation of the magnetic material of PMSM. The inductance variation will result in second-order current harmonic and periodical descent of system phase margin.
2) Two operating modes can be selected for single-phase IOBC incorporating with MPM drive. The first mode minimizes the power losses, and the second mode eliminates the torque.
3) There is an optimal zero-axis voltage for single-phase IOBC incorporating with MPM drive to maximum the dc voltage utilization. By injecting this optimal zero-axis voltage, the inverter can work in the linear modulation region.
4) The proposed P-DR regulator and P parameter adaptive control scheme can eliminate the second-order current harmonics and maintain the instantaneous phase margin of the system.

The proposed operation and control strategies have been validated using experimental tests. It shows that the proposed methods can significantly improve the power quality, efficiency and control performance of single-phase IOBC. The proposed control and operation strategies could be used in actual industrial products.

References

[1] M. Yilmaz and P. T. Krein, "Review of battery charger topologies, charging power levels, and infrastructure for plug-in electric and hybrid vehicles," *IEEE Trans. Power Electron.*, vol. 28, no. 5, pp. 2151–2169, May 2013.

[2] A. Khaligh and M. D'Antonio, "Global trends in high-power on-board chargers for electric vehicles," *IEEE Trans. Veh. Technol.*, vol. 68, no. 4, pp. 3306–3324, Apr. 2019.

[3] C. Shi, Y. Tang, and A. Khaligh, "A three-phase integrated onboard charger for plug-in electric vehicles," *IEEE Trans. Power Electron.*, vol. 33, no. 6, pp. 4716–4725, Jun. 2018.

[4] C. Shi and A. Khaligh, "A two-stage three-phase integrated charger for electric vehicles with dual cascaded control strategy," *IEEE J. Emerg. Sel. Topics Power Electron.*, vol. 6, no. 2, pp. 898–909, Jun. 2018.

[5] S. Q. Ali, D. Mascarella, G. Joos, and L. Tan, "Torque cancelation of integrated battery charger based on six-phase permanent magnet synchronous motor drives for electric vehicles," *IEEE Trans. Transp. Electrific.*, vol. 4, no. 2, pp. 344–354, Jun. 2018.

[6] I. Subotic, N. Bodo, E. Levi, M. Jones, and V. Levi, "Isolated chargers for EVs incorporating six-phase machines," *IEEE Trans. Ind. Electron.*, vol. 63, no. 1, pp. 653–664, Jan. 2016.

[7] M. S. Diab, A. A. Elserougi, A. S. Abdel-Khalik, A. M. Massoud, and S. Ahmed, "A nine-switch-converter-based integrated motor drive and battery charger system for EVs using symmetrical six-phase machines," *IEEE Trans. Ind. Electron.*, vol. 63, no. 9, pp. 5326–5335, Sep. 2016.

[8] I. Subotic, N. Bodo, and E. Levi, "An EV drive-train with integrated fast charging capability," *IEEE Trans. Power Electron.*, vol. 31, no. 2, pp. 1461–1471, Feb. 2016.

[9] F. Yu, W. Zhang, Y. Shen, and J. Mao, "A nine-phase permanent magnet electric-drive-reconstructed onboard charger for electric vehicle," *IEEE Trans. Energy Convers.*, vol. 33, no. 4, pp. 2091–2101, Dec. 2018.

[10] Z. Wang *et al.*, "A dual-channel magnetically integrated EV chargers based on double-stator-winding permanent-magnet synchronous machines," *IEEE Trans. Ind. Appl.*, vol. 55, no. 2, pp. 1941–1953, Mar./Apr. 2019.

[11] J. Gao, D. Jiang, W. Sun, and J. Chen, "A simplified single-phase integrated on-board battery charger with low EMI emission to grid," in *Proc. 21st Eur. Conf. Power Electron. Appl. (ECCE Eur.)*, 2019, pp. P.1–P.9.

[12] C. Shi, Y. Tang, and A. Khaligh, "A single-phase integrated onboard battery charger using propulsion system for plug-in electric vehicles," *IEEE Trans. Veh. Technol.*, vol. 66, no. 12, pp. 10899–10910, Dec. 2017.

[13] I. Subotic and E. Levi, "A review of single-phase on-board integrated battery charging topologies for electric vehicles," in *Proc. IEEE Workshop Elect. Mach. Des., Control Diagnosis*, 2015, pp. 136–145.

[14] H. Chen, W. Wang, and B. Huang, "Integrated driving/charging/discharging battery-powered four-phase switched reluctance motor drive with two current sensors," *IEEE Trans. Power Electron.*, vol. 34, no. 6, pp. 5019–5022, Jun. 2019.

[15] D. O. Boillat, J. W. Kolar, and J. Mühlethaler, "Volume minimization of the main DM/CM EMI filter stage of a bidirectional three-phase three-level PWM rectifier system," in *Proc. IEEE Energy Convers. Congr. Expo.*, Denver, CO, USA, 2013, pp. 2008–2019.

[16] Z. Q. Zhu and D. Howe, "Electrical machines and drives for electric, hybrid, and fuel cell vehicles," *Proc. IEEE*, vol. 95, no. 4, pp. 746–765, Apr. 2007.

[17] E. Levi, "Multiphase electric machines for variable-speed applications," *IEEE Trans. Ind. Electron.*, vol. 55, no. 5, pp. 1893–1909, May 2008.

[18] E. Levi, R. Bojoi, F. Profumo, H. A. Toliyat, and S. Williamson, "Multiphase induction motor drives—A technology status review," *IET Elect. Power Appl.*, vol. 1, no. 4, pp. 489–516, Jul. 2007.

[19] German Electrical and Electronic Manufactures' Association, "Voltage classes for electric mobility," 2014. [Online]. Available: https://www.zvei.org/fileadmin/user_upload/Presse_und_Medien/Publikationen/2014/april/Voltage_Classes_for_Electric_Mobility/Voltage_Classes_for_Electric_Mobility.pdf

[20] O. Tremblay, L. Dessaint, and A. Dekkiche, "A generic battery model for the dynamic simulation of hybrid electric vehicles," in *Proc. IEEE Veh. Power Propulsion Conf.*, Arlington, TX, USA, 2007, pp. 284–289.

[21] C. Shin, D. Kim, A. Ko, I. Won, Y. Kim, and C. Won, "The configuration of electric vehicle system using isolated DC-DC converter for a low-voltage and high-current type battery," in *Proc. 9th Int. Conf. Power Electron. ECCE Asia*, Seoul, South Korea, 2015, pp. 2796–2801.

[22] Z. Xuhui, X. Wen, Z. Feng, and G. Xinhua, "A new control strategy for bi-directional DC-DC converter in electric vehicle," in *Proc. Int. Conf. Elect. Mach. Syst.*, Beijing, China, 2011, pp. 1–4, doi: 10.1109/ICEMS.2011.6073569.

[23] R. Teodorescu, F. Blaabjerg, M. Liserre, and P. C. Loh, "Proportional-resonant controllers and filters for grid-connected voltage-source converters," *IEE Proc.—Elect. Power Appl.*, vol. 153, no. 5, pp. 750–762, Sep. 2006.

[24] F. J. Rodriguez, E. Bueno, M. Aredes, L. G. B. Rolim, F. A. S. Neves, and M. C. Cavalcanti, "Discrete-time implementation of second order generalized integrators for grid converters," in *Proc. 34th Annu. Conf. IEEE Ind. Electron.*, Orlando, FL, USA, 2008, pp. 176–181.

Jialou Gao (Student Member, IEEE) was born in Changde, Hunan Province, China, in 1996. He received the B.S. degree in electrical engineering in 2018 from the Huazhong University of Science and Technology, Wuhan, China, where he is currently working toward the M.S. degree in electrical engineering.

His research interests include control of power converters and power supplies, and high-performance motor drive systems.

Wei Sun (Member, IEEE) received the B.S. degree from Beijing Jiaotong University, Beijing, China, in 2009, and the M.S. and Ph.D. degrees from the Harbin Institute of Technology, Harbin, China, in 2012 and 2016, respectively, all in electrical engineering.

Since November 2017, he has been with Huazhong University of Science and Technology, Wuhan, China, as a Lecturer. His research interests include ac motor drives and control theory application in power electronics systems.

Dong Jiang (Senior Member, IEEE) received the B.S. and M.S. degrees in electrical engineering from Tsinghua University, Beijing, China, in 2005 and 2007, respectively. He started working toward the Ph.D. degree in high-density motor controller with the Center for Power Electronics Systems, Virginia Tech, Blacksburg, VA, USA, in 2007, and was transferred, with his advisor in 2010, to the University of Tennessee, Knoxville, TN, USA, where he received the Ph.D. degree in 2011.

From January 2012 to July 2015, he was with the United Technologies Research Center, East Hartford, CT, USA, as a Senior Research Scientist/Engineer. Since July 2015, he has been with the Huazhong University of Science and Technology, Wuhan, China, as a Professor. His research interests include power electronics and motor drives, with more than 100 published IEEE journal and conference papers in this area.

Dr. Jiang is an Associate Editor for the IEEE TRANSACTIONS ON INDUSTRY APPLICATIONS. He was the recipient of two Best Paper Awards in IEEE Conferences.

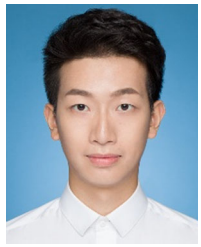

Yuanzhi Zhang (Student Member, IEEE) was born in Hunan, China. He received the B.S. degree in electrical engineering in 2017 from the Huazhong University of Science and Technology, Wuhan, China, where he is currently working toward the Ph.D. degree with the School of Electrical and Electronic Engineering.

His research interests include design and analysis of the electrical machine.

Mr. Zhang was the recipient of the Best Paper Award from the 22nd International Conference on Electrical Machines and Systems in 2019.

Ronghai Qu (Fellow, IEEE) was born in China. He received the B.E.E. and M.S.E.E. degrees from Tsinghua University, Beijing, China, 1993 and 1996, respectively, and the Ph.D. degree from the University of Wisconsin–Madison, Madison, WI, USA, in 2002, all in electrical engineering.

In 1998, he joined the Wisconsin Electric Machines and Power Electronics Consortiums, University of Wisconsin–Madison, as a Research Assistant. He became a Senior Electrical Engineer with Northland, a Scott Fetzer Company, Watertown, NY, USA, in 2002. Since 2003, he has been with the General Electric (GE) Global Research Center, Niskayuna, NY, USA, as a Senior Electrical Engineer in the Electrical Machines and Drives Laboratory. Since 2010, he has been a Professor with Huazhong University of Science and Technology, Wuhan, China. He has authored more than 230 published technical papers and is the holder of more than 50 patents/patent applications.

Dr. Qu is a Full Member of Sigma Xi. He has been the recipient of several awards from the GE Global Research Center since 2003, including the Technical Achievement and Management Awards. He was also the recipient of 2003 and 2005 Best Paper Awards, and Third Prize from the Electric Machines Committee of the IEEE Industry Applications Society (IAS), at the 2002 and 2004 IAS Annual Meeting, respectively.